

small bending and then must break, whereas columns with an aspect ratio of 80 can fully bend to touch the surface without breaking. An aspect ratio of at least 20 is needed for sufficient bending of each beam to touch its neighbors to obtain the structure shown in Fig. 4, C and D. This mechanical assessment makes it possible to design a hydrogel/nanocolumns combination that enables a desired degree of directed actuation.

We have developed hybrid architectures in which arrays of high-aspect-ratio silicon nanocolumns, either attached or free-standing, are embedded into a hydrogel film and are actuated into highly controlled, complex microstructures upon contraction and/or swelling of the polymer. The actuation is fast, reversible, reproducible, and robust. We believe that these architectures may lead to a variety of applications, including actuators, controlled reversible-pattern formation, microfluidics, reversible switching of the wetting behavior, tunable photonic structures, artificial muscles, and release systems (25).

#### References and Notes

- S. Minko, *Responsive Polymer Materials: Design and Applications* (Blackwell, Ames, IA, 2006) and references therein.
- Y. Osada, H. Okuzaki, H. Hori, *Nature* **355**, 242 (1992).
- Y. Osada, A. Matsuda, *Nature* **376**, 219 (1995).
- D. J. Beebe *et al.*, *Nature* **404**, 588 (2000).
- T. P. Russell, *Science* **297**, 964 (2002).
- J. Lahann *et al.*, *Science* **299**, 371 (2003).
- A. Lendlein, H. Y. Jiang, O. Junger, R. Langer, *Nature* **434**, 879 (2005).
- F. Chiellini *et al.*, *Macromol. Rapid Commun.* **22**, 1284 (2001).
- M. Mayer, J. Yang, I. Gittlin, D. H. Gracias, G. M. Whitesides, *Proteomics* **4**, 2366 (2004).
- T. Sun, L. Feng, X. Gao, L. Jiang, *Acc. Chem. Res.* **38**, 644 (2005) and references therein.
- K. Autum *et al.*, *Proc. Natl. Acad. Sci. U.S.A.* **99**, 12252 (2002) and references therein.
- P. Vukusic, J. R. Sambles, *Nature* **424**, 852 (2003) and references therein.
- A. K. Geim *et al.*, *Nat. Mater.* **2**, 461 (2003).
- S. B. Lee, R. Koepsel, D. B. Stolz, H. E. Warriner, A. J. Russell, *J. Am. Chem. Soc.* **126**, 13400 (2004).
- E. Delamarche, H. Schmid, B. Michel, H. Biebuyck, *Adv. Mater.* **9**, 741 (1997).
- T. N. Krupenkin, J. A. Taylor, T. M. Schneider, S. Yang, *Langmuir* **20**, 3824 (2004).
- L. Zhai, F. C. Cebeci, R. E. Cohen, M. F. Rubner, *Nano Lett.* **4**, 1349 (2004).
- S. A. Asher, in *Nanoparticles: Building Blocks for Nanotechnology*, V. M. Rotello, Ed. (Kluwer, New York, 2004), pp. 145–172.
- M. K. Maurer, I. K. Lednev, S. A. Asher, *Adv. Funct. Mater.* **15**, 1401 (2005).
- S. Park, J.-H. Lim, S.-W. Chung, C. A. Mirkin, *Science* **303**, 348 (2004).
- Materials and methods are available as supporting material on *Science Online*.
- K. S. Iyer, B. Zdyrko, H. Malz, J. Pionteck, I. Luzinov, *Macromolecules* **36**, 6519 (2003).
- B. D. Gates *et al.*, *Angew. Chem. Int. Ed.* **43**, 2780 (2004).
- E. E. Ruppert, R. S. Fox, R. B. Barnes, *Invertebrate Zoology* (Brooks Cole Thomson, Belmont, CA, ed. 7, 2004).
- In particular, our preliminary data show that these structures (i) direct the flow and particle transport (analogous to the function of cilia in organisms) and thus have potential in microfluidics, (ii) reversibly change their photonic properties and thus can be considered for tunable photonics, (iii) reversibly switch their wetting behavior from superhydrophobic in the humid environment to hydrophilic in the dry environment, and (iv) trap and release particles in microflowers.
- R. Buckminster-Fuller, *Portfolio Art News Annu.* **4**, 112 (1961). Also available at [www.rwgrayprojects.com/rbfnofes/fpapers/tensegrity/tenseg01.html](http://www.rwgrayprojects.com/rbfnofes/fpapers/tensegrity/tenseg01.html).
- D. E. Ingber, *Annu. Rev. Physiol.* **59**, 575 (1997).
- M. Defossez, *Mech. Res. Comm.* **30**, 311 (2003).
- We thank P. Kolodner, J. Weaver, I. Luzinov, and I. Sokolov for fruitful discussions. We thank R. Smith and N. Lipka for technical assistance. This work was supported in part by the Office of Naval Research, award N00014-05-1-0909.

#### Supporting Online Material

[www.sciencemag.org/cgi/content/full/315/5811/487/DC1](http://www.sciencemag.org/cgi/content/full/315/5811/487/DC1)

Materials and Methods

Figs. S1 to S5

Table S1

References

Movies S1 and S2

25 September 2006; accepted 7 December 2006

10.1126/science.1135516

# Electromechanical Resonators from Graphene Sheets

J. Scott Bunch,<sup>1</sup> Arend M. van der Zande,<sup>1</sup> Scott S. Verbridge,<sup>1</sup> Ian W. Frank,<sup>2</sup> David M. Tanenbaum,<sup>2</sup> Jeevak M. Parpia,<sup>1</sup> Harold G. Craighead,<sup>1</sup> Paul L. McEuen<sup>1\*</sup>

Nanoelectromechanical systems were fabricated from single- and multilayer graphene sheets by mechanically exfoliating thin sheets from graphite over trenches in silicon oxide. Vibrations with fundamental resonant frequencies in the megahertz range are actuated either optically or electrically and detected optically by interferometry. We demonstrate room-temperature charge sensitivities down to  $8 \times 10^{-4}$  electrons per root hertz. The thinnest resonator consists of a single suspended layer of atoms and represents the ultimate limit of two-dimensional nanoelectromechanical systems.

The miniaturization of electromechanical devices promises to be as revolutionary in the coming decades as the miniaturization of electronic devices was in the previous ones. Devices ranging from nanoscale resonators, switches, and valves have applications in tasks as diverse as information processing, molecular manipulation, and sensing. The prototypical nanoelectromechanical system (NEMS) is a nanoscale resonator, a beam of material that vibrates in response to an applied external force (1, 2). The ultimate limit would be a resonator one atom

thick, but this puts severe constraints on the material. As a single layer of atoms, it should be robust, stiff, and stable.

Graphite consists of stacked layers of graphene sheets separated by 0.3 nm and held together by weak van der Waals forces (3). It has extremely high strength, stiffness, and thermal conductivity along the basal plane. In addition, graphite can be exfoliated onto an insulating substrate, producing micron-sized graphene sheets with thicknesses down to a single atomic layer (4–8). Thus far, research on these thin graphene sheets has focused primarily on their electronic properties. We demonstrate a method of suspending single- and multilayer graphene sheets over trenches and show that such sheets can be mechanically actuated. This work also makes a detailed study of the mechanical proper-

ties of these graphene resonators, including resonance frequency, spring constant, built-in tension, and quality factor.

Suspended graphene sheets are fabricated with a peeling process similar to that reported previously (5–7). In our case, the graphene sheets are mechanically exfoliated over predefined trenches etched into a SiO<sub>2</sub> surface (Fig. 1) (9). The result is a micron-scale doubly clamped beam or cantilever clamped to the SiO<sub>2</sub> surface by van der Waals attraction. Some devices have prepatterned gold electrodes between the trenches to make electrical contact (Fig. 1, A and D).

A noncontact mode atomic force microscope (AFM) was used to quantitatively measure the thickness of the sheets on the substrate next to the trench, as shown in the inset in Fig. 1D. However, for sheets thinner than 2 to 3 nm, such measurements are unreliable (10–12). For these we used spatially resolved Raman spectroscopy to determine the number of layers (Fig. 1C) (10–12). The graphene sheet in Fig. 1B has an AFM-determined height of 0.9 nm. By comparison with previous results (10–12), the shape of the Raman peak near 2700 cm<sup>-1</sup> suggests the sheet is two layers thick over the area lying on the SiO<sub>2</sub> substrate (Fig. 1C), whereas the section suspended over the trench is a single graphene layer.

All resonator measurements are performed at room temperature and a pressure of <10<sup>-6</sup> torr unless otherwise indicated. The resonators are actuated by using either electrical (Fig. 1A) or optical modulation. In the case of electrical modulation, a time-varying radio frequency (rf)

<sup>1</sup>Cornell Center for Materials Research, Cornell University, Ithaca, NY 14853, USA. <sup>2</sup>Pomona College, Department of Physics, Claremont, CA 91711, USA.

\*To whom correspondence should be addressed. E-mail: mceuen@ccmr.cornell.edu

**Fig. 1.** (A) Schematic of a suspended graphene resonator. (B) An optical image of a double-layer graphene sheet that becomes a single suspended layer over the trench. Scale bar, 2  $\mu\text{m}$ . Each colored circle corresponds to a point where a Raman spectrum was measured. (C) Raman signal from a scan on the graphene piece. Each colored scan is data taken at each of the matching colored circles. The top scan is used as a reference and corresponds to the Raman shift of bulk graphite. (D) An optical image of few-layer ( $\sim 4$ ) graphene suspended over a trench and contacting a gold electrode. Scale bar, 1  $\mu\text{m}$ . (Inset) A line scan from tapping mode AFM corresponding to the dashed line in the optical image. It shows a step height of 1.5 nm. (E) A scanning electron microscope image of a few-layer ( $\sim 2$ ) graphene resonator. Scale bar, 1  $\mu\text{m}$ .

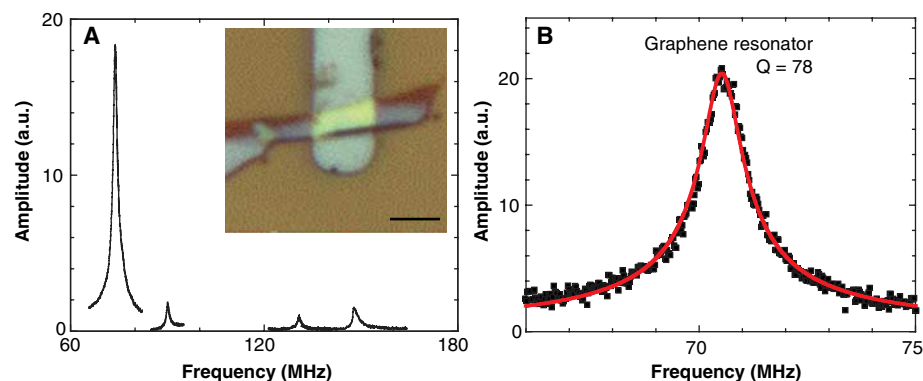
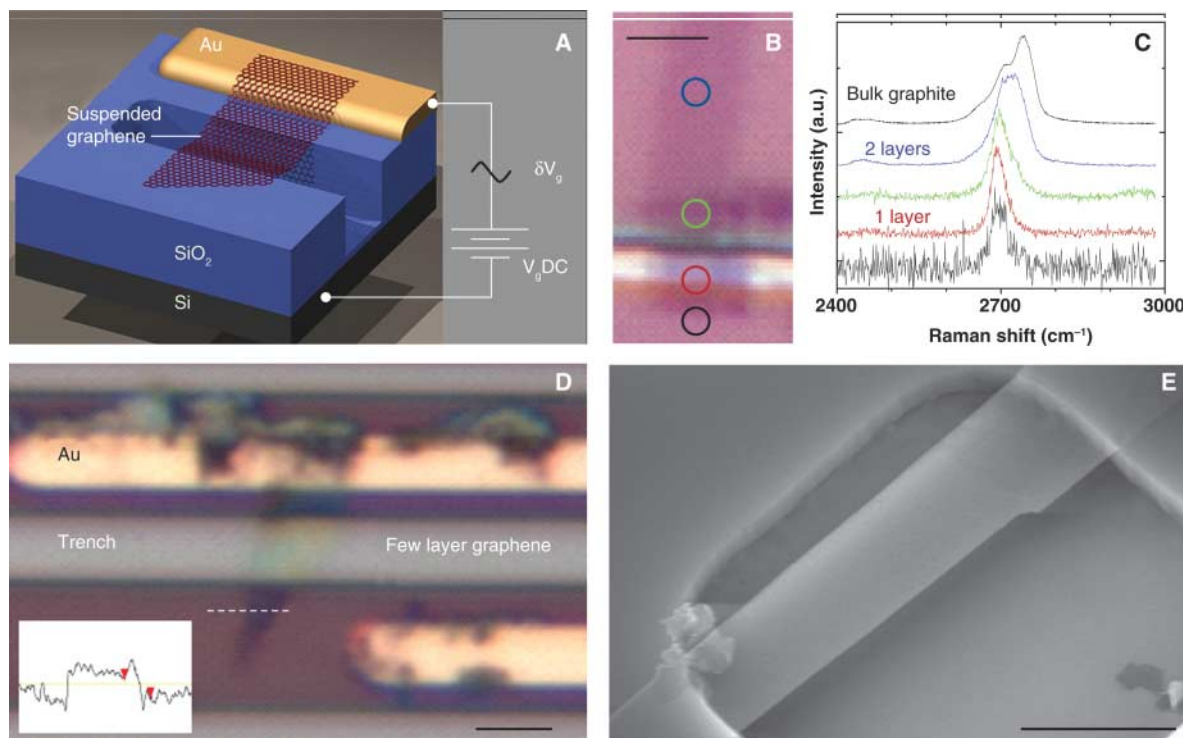


**Fig. 2.** (A) Amplitude versus frequency for a 15-nm-thick multilayer graphene resonator taken with optical drive. (Inset) An optical image of the resonator. Scale bar, 5  $\mu\text{m}$ . (B) Amplitude versus frequency taken with optical drive for the fundamental mode of the single-layer graphene resonator shown in Fig. 1B. A Lorentzian fit of the data is shown in red.

voltage  $\delta V_g$  at frequency  $f$  is superimposed on top of a constant voltage and applied to the graphene sheet. The result is an electrostatic force between the suspended graphene sheet and the substrate

$$F_{el} \approx 1/2 C_g' (V_g^{dc})^2 + C_g' V_g^{dc} \delta V_g \quad (1)$$

where  $C_g'$  is the derivative of the gate capacitance with respect to the distance to the gate, and  $V_g^{dc}$  and  $\delta V_g$  are, respectively, the dc and time-varying rf voltages applied to the gate (13). For optical actuation, the intensity of a diode laser focused on the sheet is modulated at frequency  $f$ , causing a periodic contraction/expansion of

the layer that leads to motion. In both cases, the motion is detected by monitoring the reflected light intensity from a second laser with a fast photodiode (9).

Figure 2A shows the measured amplitude versus frequency for a 15-nm-thick sheet suspended over a 5- $\mu\text{m}$  trench. Multiple resonances are observed, the most prominent one at the lowest frequency. We associate this dominant peak with the fundamental vibrational mode; its detected intensity is largest when the motion is in-phase across the entire suspended section. We will limit our discussion primarily to this fundamental mode. A fit to a Lorentzian yields a resonant frequency  $f_0 = 42$  MHz and a quality

factor  $Q = 210$ . Figure 2B shows similar results for the single-layer graphene resonator from Fig. 1B;  $f_0 = 70.5$  MHz and  $Q = 78$ . Figure 3 shows the results of measurements of 33 resonators with thicknesses varying from a single atomic layer to sheets 75 nm thick. The frequency  $f_0$  of the fundamental modes varies from 1 MHz to 170 MHz, with quality factor  $Q$  of 20 to 850.

For mechanical resonators under tension  $T$ , the fundamental resonance mode  $f_0$  is given by

$$f_0 = \{ [A(E/\rho)^{1/2} t/L^2]^2 + A^2 0.57T/\rho L^2 w t \}^{1/2} \quad (2)$$

where  $E$  is the Young's modulus;  $\rho$  is the mass density;  $t$ ,  $w$ , and  $L$  are the dimensions of the suspended graphene sheet; and the clamping coefficient,  $A$ , is 1.03 for doubly clamped beams and 0.162 for cantilevers (14). In the limit of small tension, Eq. 2 predicts that the resonance frequency  $f_0$  scales as  $t/L^2$ . Figure 3A shows the resonant frequency of the fundamental mode for resonators with  $t > 7$  nm as a function of  $t/L^2$  plotted as filled squares. Also plotted is the theoretical prediction, Eq. 2, in the limit of zero tension, for both cantilevers and beams, where we have used the known values for bulk graphite  $\rho = 2200$  kg/m<sup>3</sup> and  $E = 1.0$  TPa (3). This is a valid comparison considering the extensive theoretical and experimental work that shows the basal plane of graphite to have a similar value for  $E$  as graphene and carbon nanotubes (3, 15). To account for possible errors in  $E$ , we plot

dashed lines that correspond to values of  $E = 0.5$  TPa and 2 TPa. The data follow the predictions reasonably accurately, indicating that thicker resonators are in the bending-dominated limit with a modulus  $E$  characteristic of the bulk material. This is among the highest modulus resonators to date, greater than 53 to 170 GPa in 12- to 300-nm-thick Si cantilevers and similar to single-walled carbon nanotubes and diamond NEMS (13, 16, 17). In contrast to ultrathin Si cantilevers, the graphene resonators show no degradation in Young's modulus with decreasing thickness (17).

The resonant frequencies versus  $t/L^2$  for the resonators with  $t < 7$  nm are shown as open squares in Fig. 3A. The frequencies of these thinner resonators show more scatter, with the majority having resonant frequencies higher than predicted by bending alone. A likely explanation for this is that many of the resonators are under tension, which increases  $f_0$  (see supporting online text). The tension likely results from the fabrication process, where the friction between the graphite and the oxide surface during mechanical exfoliation stretches the graphene sheets across the trench.

The single-layer graphene resonator shown in Fig. 1B illustrates the importance of tension in the thinnest resonators. It has a fundamental frequency  $f_0 = 70.5$  MHz, much higher than the 5.4 MHz frequency expected for a tension-free beam with  $t = 0.3$  nm,  $L = 1.1$   $\mu\text{m}$ , and  $w = 1.93$   $\mu\text{m}$ . From Eq. 2, this implies that the graphene resonator has a built-in tension of  $T = 13$  nN. From the expression  $\Delta L/L = T/(EA)$ , this corresponds to a strain of  $2.2 \times 10^{-3}\%$ .

An important measure of any resonator is the normalized width of the resonance peak characterized by the quality factor  $Q = f_0/\Delta f$ . A high  $Q$  is essential for most applications because it increases the sensitivity of the resonator to external perturbation. A plot of the  $Q$  versus the thickness for all the graphene resonators (Fig. 3B) shows that there is no clear dependence of  $Q$  on thickness. This contrasts with results on thicker NEMS resonators fabricated from silicon (18). The quality factors at room temperature are lower than diamond NEMS (2500 to 3000) of similar volume and significantly lower than high-stress  $\text{Si}_3\text{N}_4$  nanostrings (200,000), yet similar to those reported in single-walled carbon nanotubes (50 to 100) (13, 16, 19). Preliminary studies on a 20-

nm-thick resonator found a dramatic increase in  $Q$  with decreasing temperature ( $Q = 100$  at 300 K to  $Q = 1800$  at 50 K). This suggests that high  $Q$  operation of graphene resonators should be possible at low temperatures.

Even when a resonator is not being driven, it will still oscillate due to thermal excitation by a root mean square (RMS) amount  $x_{\text{th}} = [k_B T / \kappa_{\text{eff}}]^{1/2}$ , where  $\kappa_{\text{eff}} = m_{\text{eff}} \omega_0^2 = 0.735 L w t \rho \omega_0^2$  is the effective spring constant of the mode (2). An example is shown in Fig. 4A, where a 5-nm-thick resonator with  $f_0 = 35.8$  MHz and  $\kappa_{\text{eff}} = 0.7$  N/m has a room-temperature thermal RMS motion of  $x_{\text{th}} = 76$  pm. For resonators for which the thermal vibrations can be measured, we use this thermal RMS motion to scale the measured photodetector voltage with resonator displacement (see supporting online text). Figure 4B shows such a rescaled plot of the displacement amplitude versus rf drive voltage. The resonator is linear up to displacements of 3 nm, or on the order of its thickness, where nonlinearities associated with additional tension are known to set in (2). This nonlinearity is characterized as a deviation from a linear increase in amplitude with driving force and accompanied by a decrease in  $Q$  (Fig. 4B).

Two applications of nanomechanical resonators are ultralow mass detection (see supporting online text) and ultrasensitive force detection. The ultimate limit on the force sensitivity is set by the thermal fluctuations in the resonator:

$$dF^f = [4 \kappa_{\text{eff}} (k_B T) / Q \omega_0]^{1/2} \quad (3)$$

For the resonator in Fig. 4A, this results in a force sensitivity of 0.9 fN/Hz<sup>1/2</sup>. From Eq. 1, this corresponds to a charge sensitivity of  $dQ^f = dF^f / dV_g^{\text{dc}} = 8 \times 10^{-4}$  e/Hz<sup>1/2</sup>, where  $d$  is the distance between the graphene sheet and the gate electrodes. This is a high sensitivity demonstrated at room temperature; at low temperatures, with the onset of higher quality factors, it could rival those of rf single-electron transistor electrometers ( $1 \times 10^{-5}$  e/Hz<sup>1/2</sup>) (20, 21). The high Young's modulus, extremely low mass, and large surface area make these resonators ideally suited

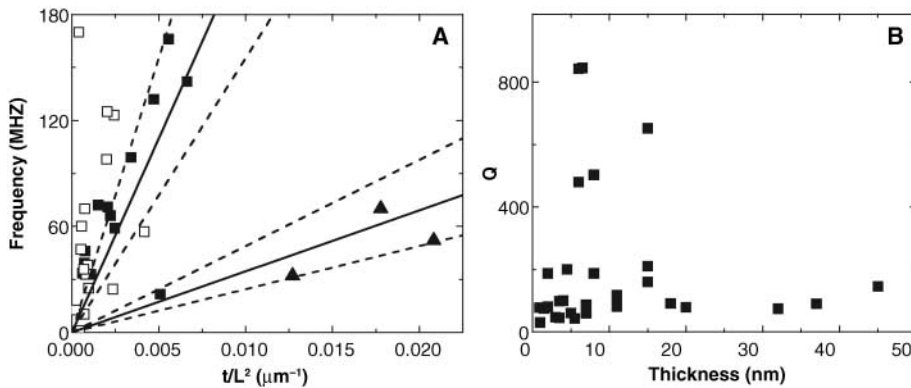


**Fig. 3.** (A) A plot showing the frequency of the fundamental mode of all the doubly clamped beams and cantilevers versus  $t/L^2$ . Cantilevers, triangles; doubly clamped beams with  $t > 7$  nm, filled squares; doubly clamped beams with  $t < 7$  nm, open squares. All thicknesses are determined by AFM. The solid line is the theoretical prediction with no tension and  $E = 1$  TPa. The dashed lines correspond to  $E = 0.5$  TPa and 2 TPa. (B) The quality factor of the fundamental mode versus thickness for all resonators measured.

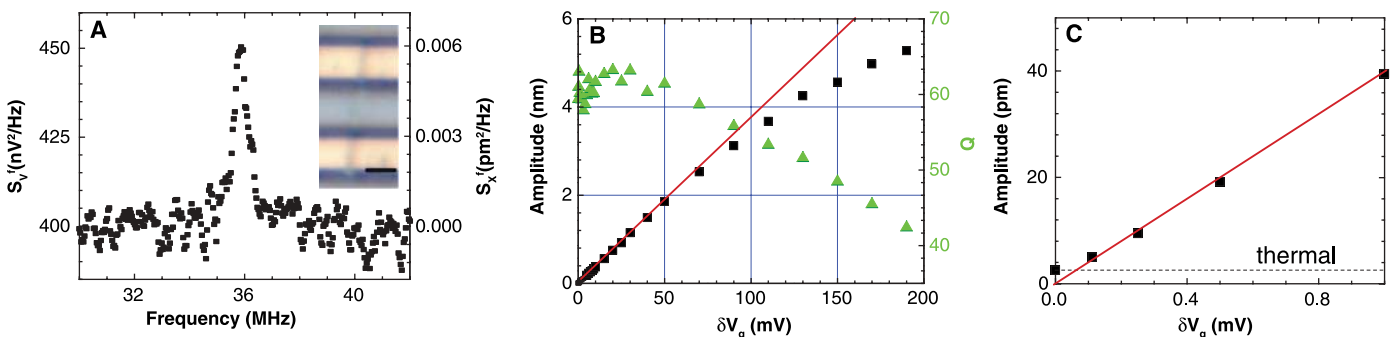


**Fig. 4.** (A) Noise power density versus frequency taken at a resolution bandwidth of 1 kHz. (Inset) An optical image of the resonator. The resonator has dimensions  $t = 5$  nm,  $L = 2.7$   $\mu\text{m}$ , and  $w = 630$  nm. Scale bar, 2  $\mu\text{m}$ . (B) Amplitude of resonance and quality factor versus  $\Delta V_g$  for  $V_g^{\text{dc}} = 2$  V. (C) Expanded view of (B) for small  $\Delta V_g$ .

for use as mass, force, and charge sensors (22–28). The application of graphene NEMS extends beyond just mechanical resonators. This robust conducting membrane can act as a nanoscale supporting structure or atomically thin membrane separating two disparate environments.

#### References and Notes

- H. G. Craighead, *Science* **290**, 1532 (2000).
- K. L. Ekinici, M. L. Roukes, *Rev. Sci. Instrum.* **76**, 061101 (2005).
- B. T. Kelly, *Physics of Graphite* (Applied Science, London; Englewood, NJ, 1981).
- M. Wilson, *Phys. Today* **59**, 21 (2006).
- K. S. Novoselov *et al.*, *Proc. Natl. Acad. Sci. U.S.A.* **104**, 10451 (2005).
- K. S. Novoselov *et al.*, *Nature* **438**, 197 (2005).
- Y. B. Zhang, Y. W. Tan, H. L. Stormer, P. Kim, *Nature* **438**, 201 (2005).
- J. S. Bunch, Y. Yaish, M. Brink, K. Bolotin, P. L. McEuen, *Nano Lett.* **5**, 287 (2005).
- Materials and methods are available as supporting material on Science Online.
- A. C. Ferrari *et al.*, *Phys. Rev. Lett.* **97**, 187401 (2006).
- A. Gupta, G. Chen, P. Joshi, S. Tadigadapa, P. C. Eklund, *Nano Lett.* **6**, 2667 (2006).
- D. Graf *et al.*, [http://arxiv.org/PS\\_cache/cond-mat/pdf/0607/0607562.pdf](http://arxiv.org/PS_cache/cond-mat/pdf/0607/0607562.pdf) (2006).
- V. Sazonova *et al.*, *Nature* **431**, 284 (2004).
- S. Timoshenko, D. H. Young, W. Weaver, *Vibration Problems in Engineering*. (Wiley, New York, ed. 4, 1974), pp. 425–427.
- D. Qian, G. J. Wagner, W. K. Liu, M. F. Yu, R. S. Ruoff, *Appl. Mech. Rev.* **55**, 495 (2002).
- L. Sekaric *et al.*, *Appl. Phys. Lett.* **81**, 4455 (2002).
- X. X. Li, T. Ono, Y. L. Wang, M. Esashi, *Appl. Phys. Lett.* **83**, 3081 (2003).
- K. Y. Yasumura *et al.*, *J. Microelectromech. Syst.* **9**, 117 (2000).
- S. S. Verbridge, J. M. Parpia, R. B. Reichenbach, L. M. Bellan, H. G. Craighead, *J. Appl. Phys.* **99**, 124304 (2006).
- R. J. Schoelkopf, P. Wahlgren, A. A. Kozhevnikov, P. Delsing, D. E. Prober, *Science* **280**, 1238 (1998).
- M. D. LaHaye, O. Buu, B. Camarota, K. C. Schwab, *Science* **304**, 74 (2004).
- B. Ilic *et al.*, *J. Appl. Phys.* **95**, 3694 (2004).
- N. V. Lavrik, P. G. Datskos, *Appl. Phys. Lett.* **82**, 2697 (2003).
- K. L. Ekinici, X. M. H. Huang, M. L. Roukes, *Appl. Phys. Lett.* **84**, 4469 (2004).
- T. Kenny, *IEEE Sensors J.* **1**, 148 (2001).
- A. N. Cleland, M. L. Roukes, *Nature* **392**, 160 (1998).
- R. G. Knobel, A. N. Cleland, *Nature* **424**, 291 (2003).
- T. P. Burg, S. R. Manalis, *Appl. Phys. Lett.* **83**, 2698 (2003).
- We thank C. Umbach and L. Bellan for help with Raman spectroscopy; R. Reichenbach for help with the laser setup and the schematic in the Supporting Online Material; and P. Kim, Y. Zhang, R. Ilic, and K. Schwab for useful discussions. This work was supported by the NSF through the Center for Nanoscale Systems and the Cornell Center for Materials Research, and by the Microelectronics Advanced Research Corporation Focused Research Center on Materials, Structures, and Devices. Sample fabrication was performed at the Cornell Nanoscale Science and Technology Facility, a National Nanotechnology Infrastructure Network node, funded by NSF.

#### Supporting Online Material

[www.sciencemag.org/cgi/content/full/315/5811/490/DC1](http://www.sciencemag.org/cgi/content/full/315/5811/490/DC1)  
Materials and Methods  
SOM Text  
Figs. S1 to S3  
References

27 October 2006; accepted 11 December 2006  
10.1126/science.1136836

## Improved Oxygen Reduction Activity on Pt<sub>3</sub>Ni(111) via Increased Surface Site Availability

Vojislav R. Stamenkovic,<sup>1,2\*</sup> Ben Fowler,<sup>3</sup> Bongjin Simon Mun,<sup>2</sup> Guofeng Wang,<sup>4</sup> Philip N. Ross,<sup>2</sup> Christopher A. Lucas,<sup>3</sup> Nenad M. Markovic<sup>1\*</sup>

The slow rate of the oxygen reduction reaction (ORR) in the polymer electrolyte membrane fuel cell (PEMFC) is the main limitation for automotive applications. We demonstrated that the Pt<sub>3</sub>Ni(111) surface is 10-fold more active for the ORR than the corresponding Pt(111) surface and 90-fold more active than the current state-of-the-art Pt/C catalysts for PEMFC. The Pt<sub>3</sub>Ni(111) surface has an unusual electronic structure (*d*-band center position) and arrangement of surface atoms in the near-surface region. Under operating conditions relevant to fuel cells, its near-surface layer exhibits a highly structured compositional oscillation in the outermost and third layers, which are Pt-rich, and in the second atomic layer, which is Ni-rich. The weak interaction between the Pt surface atoms and nonreactive oxygenated species increases the number of active sites for O<sub>2</sub> adsorption.

When a polymer electrolyte membrane fuel cell (PEMFC) is used in a demanding application such as an automobile, it must overcome the kinetic limitations on the oxygen reduction reaction (ORR), which have led to three fundamental problems (1–5). First, the substantial overpotential for the ORR (6–10) at practical operating current densities reduces the thermal efficiency well below the thermodynamic limits, typically to about 43%

at 0.7 V [versus the theoretical thermal efficiency of 83% at the reversible potential for the ORR (1.23 V)]. Second, an approximately five-fold reduction of the amount of Pt (platinum-loading) in current PEMFC stacks is needed to meet the cost requirements for large-scale automotive applications (10). Finally, the dissolution and/or loss of Pt surface area in the cathode must be greatly reduced.

These limitations could be eliminated if stable cathode catalysts, with an order of magnitude increase in the specific activity over that of state-of-the-art Pt/C catalysts, can be developed (10). In the hope that a combination of different metals would have improved catalytic activity and stability relative to those of a pure metal, the ORR has been studied on numerous bi- or multimetallic alloys (6, 8, 11–17). These studies have led to incremental improvements to catalyst perform-

ance, but large increases in activity have yet to be realized.

Rather than use a trial-and-error or combinatorial approach, we have examined selected cathode materials with well-characterized surfaces so that the mechanism of action can be attributed to a specific property (at the atomic and molecular level) of the surface under study. In this way, we can determine (i) whether the kinetics of the ORR are structure-sensitive, (ii) the composition of the topmost surface atomic layers (the segregation profile), and (iii) how alloying [usually described in terms of the ligand effect or/and ensemble effect (18–20)] alters the chemical properties of the surfaces. Similar approaches are commonly used in gas-phase catalysis (21) under ultrahigh vacuum (UHV) and near-ambient conditions, but alloy surface chemistry on single-crystal surfaces at electrochemical interfaces is relatively unexplored. These aqueous interfaces are more complex in that they necessarily contain solvent and electronic/ionic charge, and (experimentally) it is very challenging but still tractable to use in situ surface-sensitive methods to characterize potential-induced changes in the surface properties and reactivity.

We have used a combination of ex situ and in situ surface-sensitive probes and density functional theory (DFT) calculations to study the ORR on Pt<sub>3</sub>Ni(*hkl*) single-crystal surfaces, identify which surface properties govern the variations in reactivity of PtNi catalysts, and determine how surface structures, surface segregation, and intermetallic bonding affect the ORR kinetics. Well-characterized PtNi single-crystal electrode surfaces were formed and characterized with UHV methods for surface preparation and surface analysis. These surfaces were transferred into the electrochemical environment without airborne contamination, and the stability of the UHV-prepared

<sup>1</sup>Materials Science Division, Argonne National Laboratory, Argonne, IL 60439, USA. <sup>2</sup>Materials Sciences Division, Lawrence Berkeley National Laboratory, University of California, Berkeley, CA 94720, USA. <sup>3</sup>Oliver Lodge Laboratory, Department of Physics, University of Liverpool, Liverpool, L69 7ZE, UK. <sup>4</sup>Department of Chemistry and Physics, University of South Carolina, Aiken, SC 29801, USA.

\*To whom correspondence should be addressed. E-mail: vrstamenkovic@anl.gov (V.R.S.); nmmarkovic@anl.gov (N.M.M.)